

# Active Modulation of Er<sup>3+</sup> Emission Lifetime by VO<sub>2</sub> Phase-Change Thin Films

Boris Kalinic, Tiziana Cesca,\* Alessandro Lovo, Carlo Scian, Roberto Macaluso, Fabio Bovino, Roberto Li Voti, Concita Sibilìa, and Giovanni Mattei

The active modulation of optical response of quantum emitters at the nanoscale is of paramount importance to realize tunable light sources for nanophotonic devices. Herein, a thin film of phase-change material (VO<sub>2</sub>) is coupled to a 20 nm-thick silica layer embedding Er<sup>3+</sup> ions, and it is demonstrated how the active tuning of the local density of optical states near the erbium emitters provided by the thermally induced semiconductor-to-metal transition of VO<sub>2</sub> can be used to dynamically control the Er<sup>3+</sup> emission lifetime at telecom wavelength (1.54 μm). A decay rate contrast of a factor 2 is obtained between high temperature (90 °C), when VO<sub>2</sub> is metallic, and room temperature, when VO<sub>2</sub> is semiconductor, in agreement with calculations performed with the classical dipole oscillator analytical model. A hysteretic behavior is observed by measuring the Er<sup>3+</sup> lifetime as a function of the temperature, whose parameters are consistent with those of grazing incidence X-ray diffraction and optical transmittance measurements. The fractions of Er<sup>3+</sup> ions that couple with VO<sub>2</sub> in each phase at the different temperatures are determined by the analysis of the temporal decays. The results make the investigated system an optimal candidate for the development of tunable photon sources at telecom wavelength.

## 1. Introduction

Among quantum emitters, trivalent erbium ions (Er<sup>3+</sup>) are of great interest for their stable, relatively sharp, room temperature emission at 1.5 μm, which matches the window for minimum loss transmission in silica<sup>[1]</sup> Owing to this property, Er is widely used for the realization of optoelectronic devices, such as on-chip optical amplifiers, light-emitting diodes, or lasers,<sup>[2–6]</sup> and more recently for the development of single-photon sources at telecom wavelengths, which are of paramount importance for the implementation of optical fiber-based quantum networks.<sup>[7,8]</sup> Nonetheless, some limitations hamper the efficient employment of erbium in photonic devices, and in particular, its low, resonant, excitation cross section (of the order of 10<sup>–21</sup> cm<sup>2</sup>) and the long lifetime of the <sup>4</sup>I<sub>13/2</sub> excited state (of the order of 10 ms), which reduces the photon


emission rate and makes it prone to nonradiative recombination processes.<sup>[9–11]</sup> Different strategies have been then adopted during the years to overcome such limitations, as the use of metal cluster sensitizers to get broadband enhanced excitation<sup>[12–15]</sup> and the engineering of the local density of optical states (LDOS) by coupling with plasmonic or dielectric nanoarrays to enhance the radiative decay rate.<sup>[16–19]</sup> Besides this, one of the key issues for the realization of efficient optoelectronic devices for optical communication is the capability to actively modulate their optical response, possibly at ultra-high speed. To this regard, recently the active control of the erbium luminescent emission intensity has been demonstrated by near-field coupling with doped graphene monolayers<sup>[20,21]</sup> and with a phase-change material (PCM), namely a thin film of vanadium dioxide (VO<sub>2</sub>).<sup>[22,23]</sup> Owing to its semiconductor-to-metal transition (SMT) occurring slightly above room temperature (around 68 °C), VO<sub>2</sub> is definitely one of the most interesting phase-change materials and is nowadays finding more and more applications in different fields.<sup>[24,25]</sup> Moreover, the possibility to induce its phase-change transition not only thermally but also optically, with femtosecond time-scale, makes it particularly interesting for ultrafast optical switching.<sup>[26,27]</sup> Indeed, recently Cueff et al. reported a significant Er<sup>3+</sup> intensity modulation at 200 kHz exploiting VO<sub>2</sub> phase-change induced by all-optical switching.<sup>[22]</sup>

B. Kalinic, T. Cesca, A. Lovo, C. Scian, G. Mattei  
Department of Physics and Astronomy  
NanoStructures Group  
University of Padova  
via Marzolo 8, I-35131 Padova, Italy  
E-mail: tiziana.cesca@unipd.it

T. Cesca, G. Mattei  
Padua Quantum Technologies Research Center  
University of Padova  
via Gradenigo 6B, I-35131 Padova, Italy

R. Macaluso  
Department of Engineering  
University of Palermo  
viale delle Scienze, I-90128 Palermo, Italy

F. Bovino, R. Li Voti, C. Sibilìa  
Department SBAI  
Sapienza University of Roma  
via A. Scarpa 14, I-00161 Roma, Italy

 The ORCID identification number(s) for the author(s) of this article can be found under <https://doi.org/10.1002/adpr.202300242>.

© 2023 The Authors. Advanced Photonics Research published by Wiley-VCH GmbH. This is an open access article under the terms of the Creative Commons Attribution License, which permits use, distribution and reproduction in any medium, provided the original work is properly cited.

DOI: 10.1002/adpr.202300242

In the present work we investigate the coupling of a VO<sub>2</sub> thin film with Er<sup>3+</sup> emitters embedded in a 20 nm thick layer of silica from the point of view of the erbium emission lifetime, demonstrating how the modulation of the LDOS near the erbium emitters induced by the SMT of the VO<sub>2</sub> layer allows to get a significant dynamic tuning of the radiative decay rate, making this system an optimal candidate for the realization of tunable light sources integrable in nanophotonic devices.

## 2. Results and Discussion

A sketch of the sample structure is shown in **Figure 1a**. The emitting layer is a 20 nm-thick Er-doped SiO<sub>2</sub> thin film, on top of which a VO<sub>2</sub> layer (thickness of 135 nm) is deposited, with a spacer made of 20 nm of silica. In **Figure 1b** a SEM planar-view image of the VO<sub>2</sub> thin film is reported. The film presents a typical granular structure with an average grain diameter of 70 ± 20 nm, as estimated by the lognormal fit of the size probability distribution (**Figure 1c**). Grazing-incidence X-ray diffraction (GIXRD) spectra of the VO<sub>2</sub> thin film, taken in the range 22°–44° at room temperature (26 °C) and high temperature (90 °C), are reported in **Figure 1d**. The inset highlights the angular shift of the (011)–(110) VO<sub>2</sub> peaks, which is the clear signature of the VO<sub>2</sub> semiconductor-to-metal phase transition (from monoclinic *M* to rutile *R* phases).<sup>[28]</sup> **Figure 1e** shows the transmittance curves in the 400–2000 nm range, measured at low (24 °C)

and high (92 °C) temperature; the dot-dashed line indicates the 1540 nm wavelength at which the time-resolved PL measurements are taken. The thermal evolution of the structural and optical properties of the samples are summarized in **Figure 1f**, which shows the thermal hysteresis cycles during a complete heating and cooling cycle of the VO<sub>2</sub> XRD peak position (left-hand scale) and of the optical transmittance measured at λ = 1540 nm (right-hand scale).

The analysis of the GIXRD measurements was done following the approach proposed in ref. [28], i.e., assuming a continuous phase transition of the VO<sub>2</sub> from its semiconductor, monoclinic (*M*) phase at room temperature to the metallic, rutile (*R*) phase at high temperature, and fitting the VO<sub>2</sub> diffraction peak in the GIXRD scans taken at the different temperatures with a single pseudo-Voigt peak function.<sup>[28]</sup> This approach is consistent with the interpretation of the SMT transition proposed by Yao et al. in ref. [29] by temperature-dependent X-ray absorption fine structure measurements, in which the two VO<sub>2</sub> phases (*M* and *R*) undergo a continuous structural transformation. Moreover, it was demonstrated that this analysis mode provides the same results within the experimental accuracy as the approach in which the two VO<sub>2</sub> phases are assumed to co-exist and to change their relative proportion as the temperature changes during the transition, having on the other hand an intrinsic higher numerical stability.<sup>[28]</sup> For this reason, in the present case we adopted the continuous phase transition analysis mode. The data in **Figure 1f** show an almost perfect overlap of the two thermal hysteresis

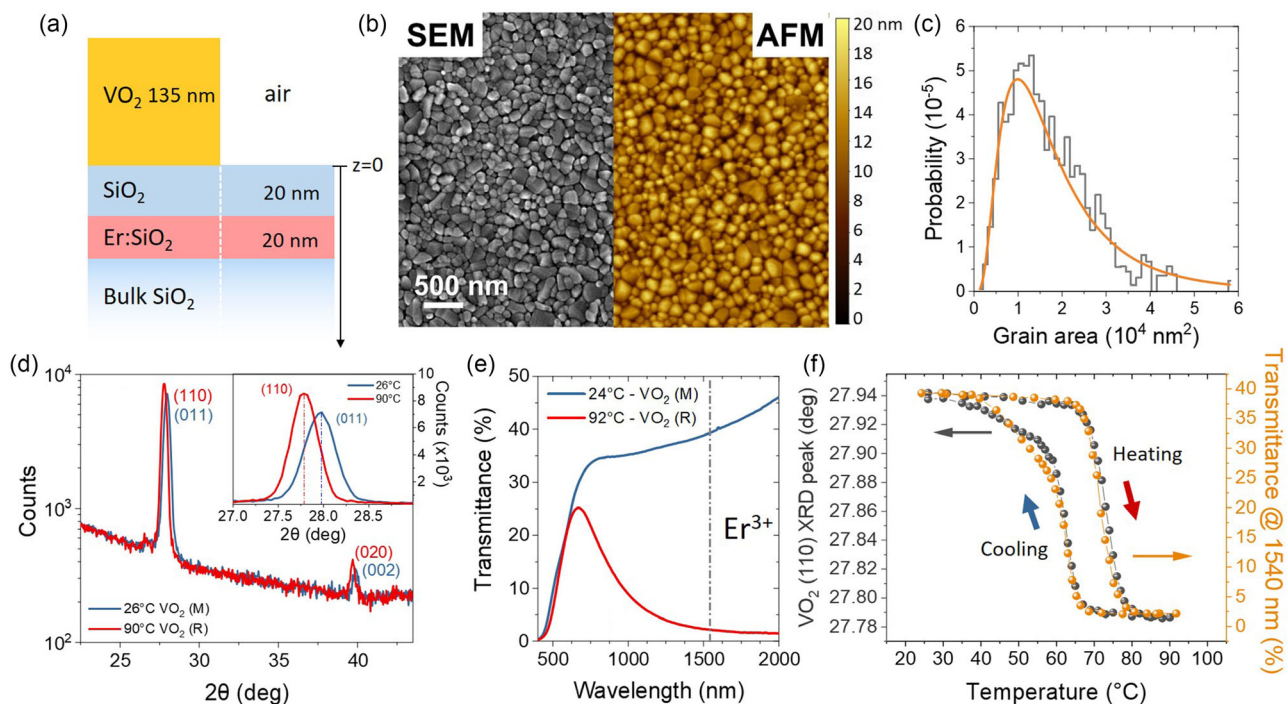


**Figure 1.** a) Sketch of the sample structure in cross-section; b) SEM (left) and AFM (right) images in planar view of the surface of the VO<sub>2</sub> layer; c) grain size distribution and the corresponding lognormal fit (red curve); d) GIXRD spectra of the VO<sub>2</sub> thin film taken at room temperature (26 °C) and high temperature (90 °C); the inset shows the shift of the VO<sub>2</sub> (011) to (110) peak as a consequence of its phase-transition from monoclinic (*M*) to rutile (*R*); e) spectral variation of the transmittance at normal incidence for the two phases (the vertical dot-dashed line indicate the spectral position of the Er<sup>3+</sup> emission at 1540 nm); f) thermal hysteresis cycles of the VO<sub>2</sub> GIXRD peaks (gray dots, left-hand scale), and of the sample transmittance at 1540 nm (orange dots, right-hand scale).

cycles. This confirms that the optical properties of the VO<sub>2</sub> layer are completely controlled by the VO<sub>2</sub> crystalline phases (the only ones detectable by GIXRD), with negligible or no contribution from possible amorphous phases, which would affect instead the optical transmittance measurements.

In both cases, the cooling branch shows a deviation from the sigmoidal trend at temperatures below the transition temperature ( $T < T_c$ ). This behaviour has been confirmed also after repeating heating-cooling cycles. This asymmetric hysteresis has been already reported in VO<sub>2</sub> thin films<sup>[30–32]</sup> and it is generally attributed either to a bimodal grain size distribution in the

film or to texturing effects in the VO<sub>2</sub> layer. These ‘defects’ may freeze a residual fraction of VO<sub>2</sub> grains in the rutile phase well below  $T_c$ , hindering, or at least slowing down, the transition back to the monoclinic phase. Considering the monomodal size distribution of the in-plane grain size distribution measured by SEM in our samples (Figure 1c), the texturing effect seems to play a dominant role in controlling the asymmetry in the hysteresis cycles, in agreement with ref. [31]. Therefore, to extract the thermal hysteresis parameters from the measurements, we used a single complementary error function (erfc) for the heating cycle and a linear combination of two erfc (double erfc) functions for the cooling one. The results of this procedure for XRD and transmittance measurements are summarized in Table 1 (for the cooling cycle the reported parameters are those of the erfc function centered at the higher temperature, i.e., the one with the highest amplitude).

The main results on the active control of the emission rate of Er<sup>3+</sup> coupled to the VO<sub>2</sub> layer are summarized in Figure 2. From the spectral point of view, very small differences emerge in the PL spectra taken at low and high temperature. As an example, Figure 2a reports the Er<sup>3+</sup> PL spectra, normalized to their maximum, of the samples with and without the VO<sub>2</sub> overlayer, measured in the range 1400–1700 nm at room and high temperature. Only a slight decrease of the emitted intensity in the region between 1400–1500 nm is observed in the sample with the VO<sub>2</sub> thin film, which can be related to a change in the electric (ED)

**Table 1.** Summary of the thermal hysteresis parameters. The transition temperatures during the heating and cooling cycles ( $T_H$  and  $T_C$ , respectively) and the corresponding transition widths ( $\sigma_H$  and  $\sigma_C$ ) are calculated from the fit of the XRD, transmittance and PL data using the erfc function for the heating cycle and the double erfc function for the cooling cycle (see text);  $\Delta T = T_H - T_C$  is the width of the thermal hysteresis.

	$T_H$ [°C]	$\sigma_H$ [°C]	$T_C$ [°C]	$\sigma_C$	$\Delta T$
GIXRD	$73.0 \pm 0.1$	$7.3 \pm 0.2$	$62.5 \pm 0.1$	$4.5 \pm 0.1$	$10.4 \pm 0.3$
$T$ (@1540 nm)	$71.7 \pm 0.1$	$6.5 \pm 0.2$	$62.6 \pm 0.1$	$4.2 \pm 0.2$	$9.5 \pm 0.3$
$\tau$	$70.9 \pm 0.3$	$10.1 \pm 0.9$	$60.2 \pm 0.3$	$7.3 \pm 0.8$	$10.7 \pm 0.4$
$f_M$	$70.0 \pm 0.4$	$9.9 \pm 1.1$	$59.4 \pm 0.4$	$7.1 \pm 0.8$	$10.6 \pm 0.4$

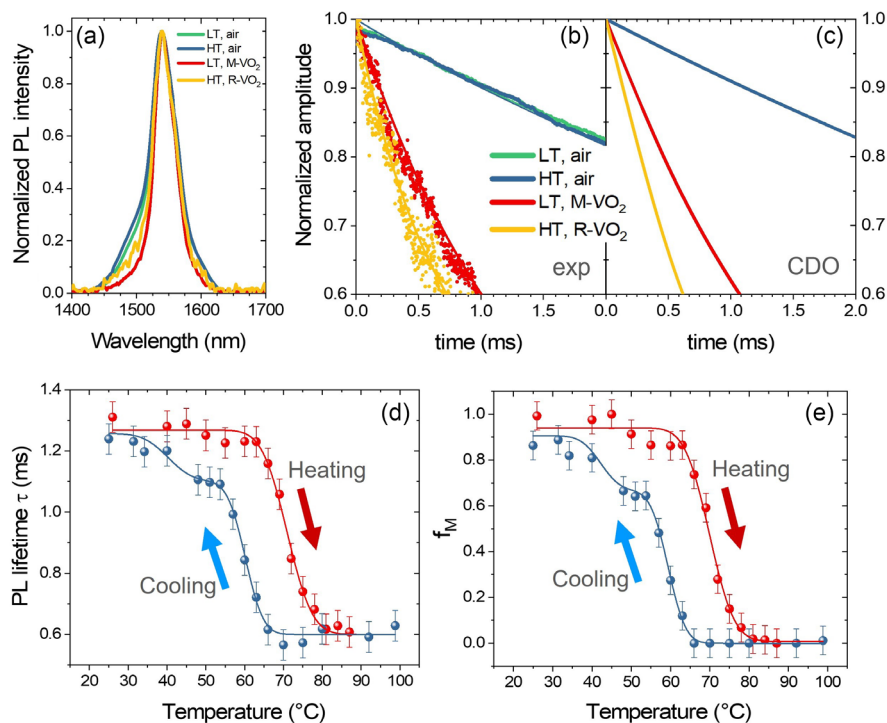


**Figure 2.** a) Room temperature Er<sup>3+</sup> PL spectra in the range 1400–1700 nm measured at low (LT, 23 °C) and high (HT, 120 °C) temperature from the Er : SiO<sub>2</sub> layer without (air) and with the VO<sub>2</sub> thin film (VO<sub>2</sub>) on top; b) normalized experimental temporal decay curves of the Er<sup>3+</sup> emission at 1540 nm measured for the samples in (a), the solid lines are the best fits to the experimental data; c) corresponding normalized temporal decay curves simulated with the CDO model; d) thermal evolution of the Er<sup>3+</sup> emission lifetime. The solid lines are the best fits to the experimental data obtained with the erfc and double erfc function for the heating and cooling cycle, respectively; e) thermal evolution of the fraction  $f_M$  of Er<sup>3+</sup> ions coupled to VO<sub>2</sub> in the monoclinic phase as a function of the sample temperature.

and magnetic (MD) dipolar relative contributions to the emitted spectrum due to the coupling with the VO<sub>2</sub> layer.<sup>[33]</sup>

Figure 2b shows the experimental temporal decay curves, normalized to their maximum, of the PL emission at 1540 nm measured at low and high temperature, respectively, from the samples with and without the VO<sub>2</sub> layer on top (the solid curves are the single exponential best fits to the experimental data). In the case of the reference sample without the VO<sub>2</sub> layer ('air', green and blue curves in Figure 2b), the temporal decay is not affected by the temperature variation and a single exponential fit gives for both samples the same value of the lifetime  $\tau_{\text{exp}}^{\text{air}} = 10.8 \pm 0.3$  ms (corresponding to a decay rate  $\Gamma_{\text{exp}}^{\text{air}} = 1/\tau_{\text{exp}}^{\text{air}} = 92 \pm 3$  s<sup>-1</sup>). On the other hand, a much shorter, temperature-dependent, lifetime is measured on the sample with the VO<sub>2</sub> layer on top ('VO<sub>2</sub>', red and yellow curves in Figure 2b):  $\tau_{\text{M}} \equiv \tau_{\text{exp}}^{26} = 1.33 \pm 0.07$  ms at 26 °C ( $\Gamma_{\text{exp}}^{26} = 750 \pm 40$  s<sup>-1</sup>) and  $\tau_{\text{R}} \equiv \tau_{\text{exp}}^{99} = 0.65 \pm 0.03$  ms at 99 °C ( $\Gamma_{\text{exp}}^{99} = 1540 \pm 70$  s<sup>-1</sup>). Moreover, the Er<sup>3+</sup> PL intensity at  $\lambda = 1540$  nm measured at room temperature ( $I_{\text{PL}}^{\text{M}}$ ) and at high temperature ( $I_{\text{PL}}^{\text{R}}$ ) is significantly modified by the change of the VO<sub>2</sub> refractive index, which affects both the radiative decay rate and the angular distribution of the emission<sup>[18,22]</sup> (which, on the basis of the CDO model, results more directed toward the sample normal when VO<sub>2</sub> is in its M phase with respect to the R one). Considering the used set-up with a NA of 0.26, a PL intensity contrast (i.e.,  $I_{\text{PL}}^{\text{M}}/I_{\text{PL}}^{\text{R}}$ ) of a factor 2 was measured at  $\lambda = 1540$  nm, in good agreement with the collection efficiencies  $\xi_{\text{M}}$  and  $\xi_{\text{R}}$  calculated with the CDO model, as reported below.

The temperature dependence of the Er<sup>3+</sup> emission rate for the sample with the VO<sub>2</sub> layer on top is due to the change of the dielectric function of the VO<sub>2</sub>, and therefore of the LDOS, upon its semiconductor-to-metal (SMT) transition. In particular, to quantify this change we defined a radiative decay contrast,  $C_{\text{r}}$ , which is the ratio between the radiative decay rate when VO<sub>2</sub> is in the rutile phase ( $\Gamma_{\text{r}}^{\text{R}}$  at high temperature) and in the monoclinic phase ( $\Gamma_{\text{r}}^{\text{M}}$  at low temperature)

$$C_{\text{r}} = \frac{\Gamma_{\text{r}}^{\text{R}}}{\Gamma_{\text{r}}^{\text{M}}} \quad (1)$$

Thus, in order to evaluate  $C_{\text{r}}$ , the radiative decay rate  $\Gamma_{\text{r}}$  for the two VO<sub>2</sub> phases has to be determined. This can be obtained from the experimentally measured decay rate considering that  $\Gamma_{\text{exp}} = \Gamma_{\text{r}} + \Gamma_{\text{nr}}$ , where  $\Gamma_{\text{nr}}$  is the non-radiative decay rate. Assuming that the sputtering deposition of the VO<sub>2</sub> thin film overlayer does not alter the intrinsic non-radiative decay rate  $\Gamma_{\text{nr}}^0$  in the Er-doped silica layer (as demonstrated in Ref. [34] for different metallic and dielectric overlayers deposited by magnetron sputtering in conditions similar to those used in the present case),  $\Gamma_{\text{nr}}^0$  can be estimated by the analysis of the decay rate in the reference sample 'air', without the VO<sub>2</sub> layer on top, as follows. First, the radiative decay rate of the reference 'air' sample (Er-doped silica layer, 20 nm thick, with 20 nm thick silica spacer and air on top) has been calculated applying the classical dipole oscillator (CDO) model for an emitter near planar interfaces,<sup>[35,36]</sup> and assuming for the intrinsic radiative decay rate in the Er-doped bulk silica the value  $\Gamma_{\text{r}}^0 = 100$  s<sup>-1</sup>.<sup>[18]</sup> Then, for the CDO model calculations, we assumed an isotropic

distribution of dipolar emitters uniformly distributed in the 20 nm thick silica layer. We considered also that the emission at 1540 nm or Er<sup>3+</sup> ions has a combined electric (ED) and magnetic dipolar (MD) character with equal weights.<sup>[33]</sup> Therefore we averaged over all the polarization directions, over the ED and MD dipolar contributions, and integrated over the depth of the emitter distribution, obtaining the normalized PL intensity as in

$$I_{\text{PL}}(t) = \frac{1}{z_1 - z_0} \int_{z_0}^{z_1} e^{-\Gamma(z)t} dz \quad (2)$$

where  $z_0 = 20$  nm and  $z_1 = 40$  nm are the initial and final depth coordinate, respectively, of the Er-doped silica layer (assuming  $z = 0$  nm at the air-spacer interface) and  $\Gamma(z)$  is the depth-dependent emission rate calculated with the CDO model following the approach described in Refs. [18,34]. The CDO calculation resulted in  $\Gamma_{\text{CDO,r}}^{\text{air}} = 69$  s<sup>-1</sup> (corresponding to  $\tau_{\text{CDO,r}}^{\text{air}} = 14.5$  ms). Finally, the intrinsic non-radiative decay rate is calculated as  $\Gamma_{\text{nr}}^0 = \Gamma_{\text{exp}}^{\text{air}} - \Gamma_{\text{CDO,r}}^{\text{air}} = 23 \pm 3$  s<sup>-1</sup> (where  $\Gamma_{\text{exp}}^{\text{air}}$  is the experimental decay rate measured for the sample without the VO<sub>2</sub> layer:  $\Gamma_{\text{exp}}^{\text{air}} = 92 \pm 3$  s<sup>-1</sup>). Therefore, the radiative decay rate of the sample with the VO<sub>2</sub> thin film, for the two VO<sub>2</sub> phases, results  $\Gamma_{\text{r}}^{\text{M}} = \Gamma_{\text{exp}}^{26} - \Gamma_{\text{nr}}^0 = 730 \pm 40$  s<sup>-1</sup> for the monoclinic phase at low temperature (26 °C) and  $\Gamma_{\text{r}}^{\text{R}} = \Gamma_{\text{exp}}^{99} - \Gamma_{\text{nr}}^0 = 1520 \pm 70$  s<sup>-1</sup> for the rutile phase at high temperature (99 °C), corresponding to a radiative decay contrast  $C_{\text{r}} = 2.1 \pm 0.2$ . This value is in good agreement with the one obtained calculating, with the same procedure described above, the effective radiative decay rates with the CDO model, which results  $C_{\text{CDO,r}} = 2.3$ .

From the radiative decay rate, the intrinsic quantum efficiency of the Er<sup>3+</sup> emission coupled to the two VO<sub>2</sub> phases can be calculated as:  $q_{\text{M}} = \Gamma_{\text{r}}^{\text{M}}/\Gamma_{\text{exp}}^{26} = 0.97 \pm 0.10$  for the monoclinic phase and  $q_{\text{R}} = \Gamma_{\text{r}}^{\text{R}}/\Gamma_{\text{exp}}^{99} = 0.99 \pm 0.09$  for the rutile one. Both these values improve the intrinsic quantum efficiency of Er-doped bulk silica, which is in our samples  $q_0 = \Gamma_{\text{r}}^0/(\Gamma_{\text{r}}^0 + \Gamma_{\text{nr}}^0) = 0.81$ . It is worth noticing that the control of the Er<sup>3+</sup> lifetime is purely governed by the change of the dielectric function of the overlayer material (i.e., the VO<sub>2</sub> thin film) and therefore no non-radiative decay channels were introduced in the emitting system and the intrinsic quantum efficiency of the Er<sup>3+</sup> emitters is preserved. Moreover, even if the variation of the Er<sup>3+</sup> lifetime due to the presence of the VO<sub>2</sub> overlayer (instead of air) is significantly larger than the relative variation induced by VO<sub>2</sub> in the two phases, rutile or monoclinic (see Equation (1)), it is important to stress that in this case it is possible to actively modulate the Er<sup>3+</sup> emission lifetime in a continuous way by modulating the VO<sub>2</sub> dielectric function exploiting the VO<sub>2</sub> semiconductor-to-metal phase-transition, as discussed below.

Deeper insights into the coupling mechanism between the Er<sup>3+</sup> ions and the VO<sub>2</sub> thin film can be obtained by studying the evolution of the Er<sup>3+</sup> emission lifetime, in the sample with the VO<sub>2</sub> layer, as a function of the temperature around the VO<sub>2</sub> SMT phase transition. To this aim, we performed time-resolved PL measurements of the Er:SiO<sub>2</sub>+VO<sub>2</sub> sample, doing a complete heating and cooling cycle in the temperature range 26°–90 °C. In Figure 2d we report the trend of the lifetime

$\tau(T)$  obtained by the exponential fits of the temporal decay curves as a function of the temperature. The thermal evolution of  $\tau(T)$  is perfectly correlated to the thermal hysteresis of the VO<sub>2</sub> layer observed both with GIXRD and optical transmittance measurements (Figure 1f), showing also the same asymmetry between heating and cooling cycles. Therefore, to extract the hysteresis parameters for  $\tau(T)$  we adopted the same fitting procedure used for GIXRD and transmittance cycles, i.e., a single erfc function for the heating and a double erfc function for the cooling cycle, respectively. The results are reported in Table 1. The thermal evolution of  $\tau(T)$  in Figure 2d can be interpreted in the frame of a continuous phase transition of the VO<sub>2</sub> film, which gives rise to a continuous modulation of the emission lifetime of Er<sup>3+</sup> ions coupled with the VO<sub>2</sub> thin film.

On the other hand, we can gain complementary information by re-interpreting the phase transition as one in which the two VO<sub>2</sub> phases (monoclinic and rutile) actually co-exist with different relative fractions  $f_M$  and  $f_R$ , respectively (with the condition  $f_M(T) + f_R(T) = 1$  at each temperature). In this case, to analyze the temporal decay of the PL intensity  $I_{PL}(t)$  taken at the different temperatures, a double-exponential function is used, as in

$$I_{PL}(t; T) = A_M(T) e^{-t/\tau_M} + A_R(T) e^{-t/\tau_R} \quad (3)$$

where the two exponential terms represent the contribution to the measured PL intensity of the emission coming from two independent populations of Er<sup>3+</sup> ions coupled to VO<sub>2</sub> in the monoclinic (M) and rutile (R) phase, with lifetime  $\tau_M = \tau_{exp}^{26} = 1.33 \pm 0.07$  ms and  $\tau_R = \tau_{exp}^{99} = 0.65 \pm 0.03$  ms, respectively.

A quantitative estimation of the fraction of Er<sup>3+</sup> ions in each population can be obtained by the analysis of the pre-factors of the exponential terms in Equation (3). To do so, let's consider that for steady-state conditions and in the limit of a low incident photon flux (i.e., in the linear regime,  $\sigma\phi\tau \ll 1$ ),<sup>[14]</sup> Equation (3) can be rewritten in the form

$$I_{PL}(t; T) = C[f_M(T) q_M \xi_M e^{-t/\tau_M} + f_R(T) q_R \xi_R e^{-t/\tau_R}] \quad (4)$$

with  $C = K\sigma\phi N_{Er}^*$ , where  $K$  is a proportionality constant that accounts for the collection efficiency of the PL setup,  $\sigma$  is the Er<sup>3+</sup> excitation cross-section at 520 nm ( $\approx 10^{-21}$  cm<sup>2</sup>),  $\phi$  is the incident photon flux ( $\approx 10^{19}$  photons s<sup>-1</sup> cm<sup>-2</sup>) and  $N_{Er}^*$  is the population of active Er<sup>3+</sup> ions in the Er-doped silica layer.  $q_M$  and  $q_R$  are the intrinsic quantum efficiencies for each population of active Er<sup>3+</sup> ions, and  $\xi_M$  and  $\xi_R$  are the corresponding collection efficiencies, i.e., the efficiency of photon emission within the numerical aperture (NA) of the collection lens in the PL setup (in our case NA = 0.26) for each phase of the VO<sub>2</sub> layer. The collection efficiencies were calculated with the CDO model, as in Refs. [18,34], obtaining  $\xi_M = 4.6 \times 10^{-3}$  and  $\xi_R = 2.2 \times 10^{-3}$  for the monoclinic and rutile phases, respectively.

The fractions of Er<sup>3+</sup> emitters in the two populations,  $f_M, f_R$ , can be then calculated by the ratio of the first two exponential terms in Equation (3) and (4), and considering the condition  $f_M + f_R = 1$ . In this way a system of two equations is obtained in which the only unknown quantities are  $f_M$  and  $f_R$ . Figure 2e reports the solutions of this system for  $f_M(T)$  as a function of the

heating and cooling cycles, showing the same asymmetric hysteresis, whose parameters are reported in Table 1. An overall good agreement between all the measurements is found (minor differences can be related to small possible thermal calibrations in the different setups used for the measurements). This result confirms that the observed reversible active control of the Er<sup>3+</sup> emission is related to the SMT transition of VO<sub>2</sub>.

### 3. Conclusion

In the present work we demonstrated that the coupling with a phase-change material, namely a VO<sub>2</sub> thin film, can be used to actively and reversibly control the decay rate of trivalent erbium emitters embedded in a silica layer coupled in near-field. The observed modulation of the erbium emission lifetime is a consequence of the variation of the LDOS near the erbium emitters induced by the refractive index modulation due to the SMT of the VO<sub>2</sub> thin film. A complete hysteresis cycle is measured by varying the sample temperature in the range between room temperature and 100 °C. The hysteresis parameters are consistent with those obtained by GIXRD and transmittance measurements of the VO<sub>2</sub> layer as a function of the temperature, confirming the active role provided by the phase-change material. A radiative emission rate contrast  $C_r$  of about 2 is measured for the two extreme conditions of low and high temperature, in good agreement with the results of the calculations done with the classical dipole oscillator (CDO) model. Moreover, from the analysis of the photoluminescence (PL) temporal decay curves it was possible to determine the relative fraction of Er<sup>3+</sup> ions coupled with the two phases of the VO<sub>2</sub> thin film, semiconductor (monoclinic, M) or metallic (rutile, R), at the different temperatures. This is consistent with the description of the VO<sub>2</sub> SMT in which the two VO<sub>2</sub> phases coexist at all the temperatures, with different relative proportion.

The presented results demonstrate the potential of the proposed system for the realization of actively tunable light sources at telecom wavelengths to be integrated in nanoscale devices. Moreover, in perspective the possibility to induce the SMT transition in the VO<sub>2</sub> thin film also optically, e.g., with fs pulse time-scales, paves the way for an ultrafast control of the radiative decay rate of quantum emitters to be used as advanced light sources.

### 4. Experimental Section

**Samples Fabrication:** The samples were fabricated by sequential sputtering depositions to realize a multilayer structure. The apparatus used was a confocal magnetron sputtering system equipped with three torches, one worked in direct current (DC) and two at radio-frequency (RF), mounting 2"-diameter targets. A sketch of the samples' structure is shown in Figure 1a. The silica substrate (HSQ100 by Heraeus) was first cleaned in an acid piranha solution (H<sub>2</sub>SO<sub>4</sub>: H<sub>2</sub>O<sub>2</sub>, 3:1) at 80 °C for 1 h. Then, a 20 nm-thick Er-doped silica layer was deposited onto the silica substrate by co-sputtering of Er and SiO<sub>2</sub>. The DC source was used for sputtering a metallic Er target at the power of 3 W, while one RF source was used for the deposition of silica from an amorphous SiO<sub>2</sub> target at the power of 300 W. The co-deposition was performed in an Ar (16 sccm) + O<sub>2</sub> (0.3 sccm) mixture, at a working pressure of  $5 \times 10^{-3}$  mbar. The power of the two torches was set to get an Er concentration in the films of the order of 0.5 at% (i.e., below the concentration quenching limit), as measured by Rutherford backscattering spectrometry on reference samples deposited on silicon

substrates in the same experimental conditions. Then a silica spacer of 20 nm was deposited on them by RF sputtering with Ar (8.7 sccm,  $5 \times 10^{-3}$  mbar) at 100 W. These samples (used as a reference and labeled as “air,” since the emitting layer was coupled to air) were thermally annealed in an oven in vacuum (at a pressure of about  $10^{-5}$  mbar) at 850 °C for 2 h. This annealing treatment was necessary to improve the octahedral coordination of oxygen atoms around the erbium ions in the silica matrix and thus the activation of the  $\text{Er}^{3+}$  luminescent centers. PL measurements were performed to characterize the erbium emission properties in these samples.

Subsequently, for each sample half of the surface was masked, and the samples were placed again inside the sputtering system in order to deposit the active layer of  $\text{VO}_2$  (135 nm thick) on top of the silica spacer (samples labeled as ‘ $\text{VO}_2$ ’). In this case, a metallic vanadium target was mounted on the DC source and sputtered with Ar (12 sccm) +  $\text{O}_2$  (1.3 sccm) at a pressure of  $5.4 \times 10^{-3}$  mbar, with a power of 130 W. After the deposition, the samples were thermally annealed in  $\text{N}_2$  flux ( $100 \text{ NI h}^{-1}$ ) at 570 °C for 2 h to promote the crystallization of the  $\text{VO}_2$  thin film. The thickness of the  $\text{SiO}_2$  spacer was chosen in order to maximize the radiative decay rate contrast (Equation (1)) of the erbium emission lifetime when  $\text{VO}_2$  was in the rutile (R) or monoclinic (M) phase, whereas the thickness of the  $\text{VO}_2$  thin film was selected in order to have an optically thick layer.

**Morphological and Structural Characterizations:** The surface morphology of the samples was characterized by scanning electron microscopy (SEM) and atomic force microscopy (AFM). SEM measurements were performed with a field-emission scanning electron microscope (FE-SEM, Zeiss Sigma HD) operating in the 0.2–30 kV range, while an NT-MDT (Solver-PRO) atomic force microscope was used for the AFM characterizations. The atomic force microscope was also used to measure the thickness of the deposited layers.

X-ray diffraction (XRD) measurements were taken in grazing incidence (GIXRD, with grazing angle  $\omega = 0.5^\circ$ ) with a Panalytical X’Pert Pro high-resolution diffractometer working in parallel beam geometry with a  $\text{CuK}_\alpha$  source. The system was equipped with an Anton Paar DHS900 heatable specimen holder to perform in situ XRD scans as a function of the temperature. The scans were taken in  $\text{N}_2$  flux, varying the temperature in the range 26–90 °C at steps of 2 °C, with heating (cooling) rate of  $0.4^\circ\text{C min}^{-1}$ . At each temperature, the system was thermalized for 5 min before starting the X-ray measurement. The temperature was monitored by the internal thermocouple of the DHS900 system mounted in close proximity to the back of the sample. An external calibrated PT100 thermoresistance placed in direct contact with the sample’s surface was also used to check possible differences between the nominal temperature of the DHS900 system and the actual temperature at the sample’s surface (where the  $\text{VO}_2$  layer was deposited): the values were in agreement within the experimental uncertainties, ruling out possible differences due to the thermal isolation of the silica substrate.

**Optical Characterizations:** The  $\text{Er}^{3+}$  emission properties at 1540 nm (involving the  $^4I_{13/2} \rightarrow ^4I_{15/2}$   $\text{Er}^{3+}$  transition) were characterized at different temperatures in the range between room temperature and 100 °C by wavelength- and time-resolved PL measurements. The pump laser was a fiber-coupled cw diode laser (Integrated Optics) emitting at 520 nm (in resonance with the  $^4I_{15/2} \rightarrow ^2H_{11/2}$   $\text{Er}^{3+}$  absorption transition), mechanically modulated by a chopper at a frequency of 13 Hz. The laser power is set at 50 mW during the measurements. The sample is placed on a sample holder inside a cryostat and maintained in vacuum by a turbo-molecular pump. Heating and cooling cycles are performed varying the temperature in the range 26–100 °C at steps of 3 or 5 °C. The sample is maintained at each temperature for 5 min to assure its thermalization. The laser impinges on the sample from the silica substrate on the back side at an angle of  $30^\circ$ , and the  $\text{Er}^{3+}$  PL emission is collected from the same side normally to the sample’s surface with a converging lens ( $\text{NA} = 0.26$ ). The PL signal is then spectrally analyzed by a single-grating monochromator and recorded with a  $\text{N}_2$ -cooled photomultiplier tube (Hamamatsu R5509-72) coupled with a lock-in amplifier. Time-resolved PL measurements are taken by setting the detected wavelength at

1540 nm and recording the temporal decay of the PL intensity with a digital oscilloscope (Tektronix TDS 7104).

The thermal transition of the  $\text{VO}_2$  thin film from its room temperature monoclinic phase (M, semiconducting) to the high-temperature rutile one (R, metallic) is optically monitored with a Jasco V670 spectrophotometer, recording transmittance spectra of the samples in the VIS-IR range (400–2000 nm) at different temperature. Heating and cooling cycles are performed in the range 24–92 °C at steps of 2 °C.

The dielectric function of the deposited  $\text{VO}_2$  layer is experimentally measured by using a J. Woolham V-VASE spectroscopic ellipsometer. The measurements are performed both at room temperature and at 100 °C. At 1540 nm ( $\text{Er}^{3+}$  emission wavelength), the dielectric functions result in  $\epsilon_M = 9.7 + i2.3$  at room temperature and  $\epsilon_R = -7.5 + i11.6$  at 100 °C, respectively.

## Acknowledgements

This work was performed in the framework of the PNRM Project “METEORE” (contract n. 564, year 2021) funded by the Italian Ministry of Defense and was supported in part by the Italian MUR Departments of Excellence grant 2023-2027 “Quantum Frontiers.”

## Conflict of Interest

The authors declare no conflict of interest.

## Data Availability Statement

The data that support the findings of this study are available on request from the corresponding author. The data are not publicly available due to privacy or ethical restrictions.

## Keywords

decay rate control, erbium emission, phase-change materials, semiconductor-to-metal transition, vanadium dioxide

Received: August 13, 2023

Revised: October 31, 2023

Published online:

- [1] K. Binnemans, *Chem. Rev.* **2009**, *109*, 4283.
- [2] J. Rönn, W. Zhang, A. Autere, X. Leroux, L. Pakarinen, C. Alonso-Ramos, A. Säynätjoki, H. Lipsanen, L. Vivien, E. Cassan, Z. Sun, *Nat. Commun.* **2019**, *10*, 432.
- [3] J. Chen, W. Zhu, Y. Gao, D. Yang, X. Ma, *Opt. Express* **2019**, *27*, 30919.
- [4] J. Hong, H. Wen, J. He, J. Liu, Y. Dan, J. W. Tomm, F. Yue, J. Chu, C. Duan, *Photon. Res.* **2021**, *9*, 714.
- [5] S. Zhu, L. Shi, B. Xiao, X. Zhang, X. Fan, *ACS Photonics* **2018**, *5*, 3794.
- [6] N. Li, D. Vermeulen, Z. Su, E. S. Magden, M. Xin, N. Singh, A. Ruocco, J. Notaros, C. V. Poulton, E. Timurdogan, C. Baiocco, M. R. Watts, *Opt. Express* **2018**, *26*, 16200.
- [7] A. Dibos, M. Raha, C. Phenicie, J. Thompson, *Phys. Rev. Lett.* **2018**, *120*, 243601.
- [8] A. Alizadehkhaledi, A. L. Frencken, F. C. J. M. van Veggel, R. Gordon, *Nano Lett.* **2020**, *20*, 1018.
- [9] G. Liu, B. Jacquier, *Spectroscopic Properties of Rare Earths in Optical Materials*, Springer Berlin, Heidelberg **2005**.
- [10] A. Polman, *J. Appl. Phys.* **1997**, *82*, 1.

- [11] T. Cesca, C. Maurizio, B. Kalinic, G. Perotto, P. Mazzoldi, E. Trave, G. Battaglin, G. Mattei, *Opt. Express* **2012**, *20*, 16639.
- [12] M. Eichelbaum, K. Rademann, *Adv. Funct. Mater.* **2009**, *19*, 2045.
- [13] T. Cesca, B. Kalinic, C. Maurizio, N. Michieli, C. Scian, G. Mattei, *RSC Adv.* **2016**, *6*, 99376.
- [14] T. Cesca, B. Kalinic, C. Maurizio, C. Scian, G. Battaglin, P. Mazzoldi, G. Mattei, *ACS Photonics* **2015**, *2*, 96.
- [15] C. Maurizio, T. Cesca, G. Perotto, B. Kalinic, N. Michieli, C. Scian, Y. Joly, G. Battaglin, P. Mazzoldi, G. Mattei, *Nanoscale* **2015**, *7*, 8968.
- [16] N. Michieli, B. Kalinic, C. Scian, T. Cesca, G. Mattei, *ACS Photonics* **2018**, *5*, 2189.
- [17] B. Kalinic, T. Cesca, I. G. Balasa, M. Trevisani, A. Jacassi, S. A. Maier, R. Sapienza, G. Mattei, *ACS Photonics* **2023**, *10*, 534.
- [18] B. Kalinic, T. Cesca, S. Mignuzzi, A. Jacassi, I. G. Balasa, S. A. Maier, R. Sapienza, G. Mattei, *Phys. Rev. Appl.* **2020**, *14*, 014086.
- [19] G. Perotto, V. Bello, T. Cesca, G. Mattei, P. Mazzoldi, G. Pellegrini, C. Scian, *Nucl. Instrum. Methods Phys. Res., Sect. B* **2010**, *268*, 3211.
- [20] K. J. Tielrooij, L. Orona, A. Ferrier, M. Badioli, G. Navickaite, S. Coop, S. Nanot, B. Kalinic, T. Cesca, L. Gaudreau, Q. Ma, A. Centeno, A. Pesquera, A. Zurutuza, H. de Riedmatten, P. Goldner, F. J. García de Abajo, P. Jarillo-Herrero, F. H. L. Koppens, *Nat. Phys.* **2015**, *11*, 281.
- [21] D. Cano, A. Ferrier, K. Soundarapandian, A. Reserbat-Plantey, M. Scarafagio, A. Tallaire, A. Seyeux, P. Marcus, H. de Riedmatten, P. Goldner, F. H. L. Koppens, K.-J. Tielrooij, *Nat. Commun.* **2020**, *11*, 4094.
- [22] S. Cuff, D. Li, Y. Zhou, F. J. Wong, J. A. Kurvits, S. Ramanathan, R. Zia, *Nat. Commun.* **2015**, *6*, 8636.
- [23] E. Petronijevic, M. Centini, T. Cesca, G. Mattei, F. A. Bovino, C. Sibilìa, *Opt. Express* **2019**, *27*, 24260.
- [24] Y. Ke, S. Wang, G. Liu, M. Li, T. J. White, Y. Long, *Small* **2018**, *14*, 1802025.
- [25] K. Liu, S. Lee, S. Yang, O. Delaire, J. Wu, *Mater. Today* **2018**, *21*, 875.
- [26] K. Appavoo, B. Wang, N. F. Brady, M. Seo, J. Nag, R. P. Prasankumar, D. J. Hilton, S. T. Pantelides, R. F. Haglund, *Nano Lett.* **2014**, *14*, 1127.
- [27] S. Lysenko, A. Rúa, V. Vikhnin, F. Fernández, H. Liu, *Phys. Rev. B* **2007**, *76*, 035104.
- [28] T. Cesca, C. Scian, E. Petronijevic, G. Leahu, R. Li Voti, G. Cesarini, R. Macaluso, M. Mosca, C. Sibilìa, G. Mattei, *Nanoscale* **2020**, *12*, 851.
- [29] T. Yao, X. Zhang, Z. Sun, S. Liu, Y. Huang, Y. Xie, C. Wu, X. Yuan, W. Zhang, Z. Wu, G. Pan, F. Hu, L. Wu, Q. Liu, S. Wei, *Phys. Rev. Lett.* **2010**, *105*, 226405.
- [30] V. A. Klimov, I. O. Timofeeva, S. D. Khanin, E. B. Shadrin, A. V. Ilinskii, F. Silva-Andrade, *Tech. Phys.* **2002**, *47*, 1134.
- [31] M. Currie, V. D. Wheeler, B. Downey, N. Nepal, S. B. Qadri, J. A. Wollmershauser, J. Avila, L. Nyakiti, *Opt. Mater. Express* **2019**, *9*, 3717.
- [32] M. E. Uslu, I. B. Misirlioglu, K. Sendur, *Opt. Mater. Express* **2018**, *8*, 2035.
- [33] D. Li, S. Karaveli, S. Cuff, W. Li, R. Zia, *Phys. Rev. Lett.* **2018**, *121*, 227403.
- [34] B. Kalinic, T. Cesca, N. Michieli, C. Scian, G. Battaglin, P. Mazzoldi, G. Mattei, *J. Phys. Chem. C* **2015**, *119*, 6728.
- [35] R. R. Chance, A. Prock, R. Silbey, in *Advances in Chemical Physics* (Eds: I. Prigogine, S. A. Rice), Vol. 37, John Wiley & Sons, New York **1978**.
- [36] W. Barnes, *J. Mod. Opt.* **1998**, *45*, 661.